Journal of Nuclear Materials 505 (2018) 1–6

Contents lists available at ScienceDirect

Journal of Nuclear Materials

journal homepage: www.elsevier.com/locate/jnucmat

The formation and structure of Fe-Mn-Ni-Si solute clusters and G-phase precipitates in steels

D.J.M. King [a, *], P.A. Burr [b], S.C. Middleburgh [c, e], T.M. Whiting [a], M.G. Burke [d], M.R. Wenman [a]

[a] Centre for Nuclear Engineering, Imperial College London, South Kensington, London, SW7 2AZ, United Kingdom
[b] School of Electrical Engineering, University of New South Wales, Kensington, 2052, NSW, Australia
[c] Westinghouse Electric Sweden AB, SE-721 63 Västerås, Sweden
[d] Materials Performance Centre, The University of Manchester, Sackville Street Campus, Manchester, M13 9PL, UK
[e] Nuclear Futures Institute, Bangor University, Dean Street, Bangor, Wales, LL57 1UT, UK

GRAPHICAL ABSTRACT

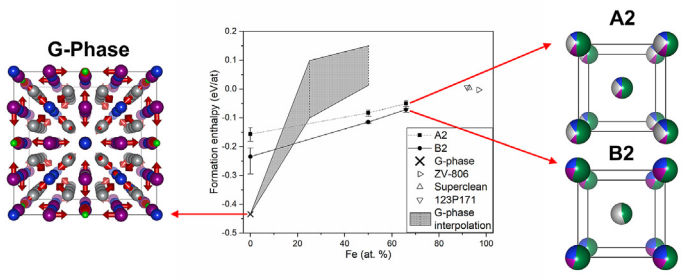

ARTICLE INFO

Article history:
Received 4 January 2018
Received in revised form
17 March 2018
Accepted 28 March 2018
Available online 30 March 2018

Keywords:
Density functional theory
RPV steels
Duplex steels
Ferritic
Solute clustering

ABSTRACT

Solute clustering and G-phase precipitation cause hardening phenomena observed in some low alloy and stainless steels, respectively. Density functional theory was used to investigate the energetic driving force for the formation of these precipitates, capturing temperature effects through analysis of the system's configurational and magnetic entropies. It is shown that enrichment of Mn, Ni and Si is thermodynamically favourable compared to the dilute ferrite matrix of a typical A508 low alloy steel. We predict the ordered G-phase to form preferentially rather than a structure with B2-type ordering when the Fe content of the system falls below 10–18 at. %. The B2 → G-phase transformation is predicted to occur spontaneously when vacancies are introduced into the B2 structure in the absence of Fe.

1. Introduction

An understanding of the behaviour of solute atoms within steel components is of great importance to many industries. This is especially true when the steels are exposed to elevated temperatures (573–773 K) for long periods of time (>1 year), as

* Corresponding author. Flat 18, Crewkerne Court, Bolingbroke Walk, SW11 3NF, United Kingdom.
E-mail address: daniel.king@imperial.ac.uk (D.J.M. King).

https://doi.org/10.1016/j.jnucmat.2018.03.050
0022-3115/

intermetallic compounds are found to precipitate – some embrittling the alloy [1–3]. In the nuclear sector, austenitic stainless steels are commonly used for the primary coolant water pipes [4], reactor pressure vessel (RPV) cladding [5] and low alloy ferritic steels are used for the RPV themselves. The continued structural integrity of the RPV is vital for the extended and continued operation of light water reactors as it is unfeasible to replace them during the reactor's operational lifetime [6]. Solute clustering, due to prolonged neutron irradiation, is a known phenomenon that occurs in RPV steels and contributes to their embrittlement potentially limiting the life of the power plant [7]. However, a mechanistic understanding of the conditions and exact nature of their occurrence is not agreed upon [8]. Further, debate continues as to whether current dose-damage relationships [9,10] already include the hardening from these clusters or if additional hardening terms may be required. Past studies have observed the clusters to consist of solute elements Cu, Mn, Ni and Si in the body-centred cubic (BCC) Fe matrix [11–13]. In efforts to avoid these features, the Cu content have been significantly reduced (as seen in A508 steels) [14]; however, Mn, Ni and Si are still observed to cluster. These clusters are sometimes termed as Mn-Ni-rich precipitates (MNPs) [15] or Mn-Ni-Si precipitates (MNSPs) [16]. However, there is some contention around their designation as "precipitates" due to the disagreement of their stability and structure [8]. The argument for their designation as a precipitate [17], suggests that the solutes form an $Fm\bar{3}m$ $D8_a$ (ordered Th_6Mn_{23}) intermetallic compound, commonly referred to as the G-phase [18]. This is quite plausible as in high alloy duplex stainless steels the G-phase is seen to precipitate in the ferritic phase, as a consequence of long thermal ageing (10,000 h at 673 K) [19,20]. Difficulties in confirming this hypothesis occur as experimental techniques commonly used to analyse the solute clusters, such as atom probe tomography (APT) [21] and small angle neutron scattering (SANS), do not sufficiently elucidate the clusters' crystal structures. Publications using techniques better suited to crystal structure identification, such as, transmission electron microscopy (TEM) electron diffraction or high resolution TEM have not revealed evidence of the G-phase in irradiated RPV steels to-date.

The current study is concerned with the system at equilibrium. Density functional theory (DFT) is used to study the energetic preference for clustering, A2 disorder and partial ordering, analogous to B2 and $D0_3$ (strukturbericht notation) of Mn, Ni and Si to occur in the BCC Fe lattice and the driving force for transformation to the G-phase.

2. Methodology

2.1. Density functional theory

A plane-wave density functional theory method was used, as implemented in the Vienna Ab initio Simulation Package (VASP) [22]. Developer provided pseudopotentials, using the projector augmented wave method (PAW) [23], were used to represent the electronic structure of each element. Semi-core *p* states were considered valence electrons for Fe (14), Ni (16) and Mn (13) and a standard number for Si (4).

The *k*-points, cut-off energy and lattice parameters of all elements in their ground state structures (BCC-Fe, FCC-Ni, α-Mn, diamond-Si) were converged and used as reference states. It was determined that a real space *k*-point density of <0.02 $Å^{-3}$ and a cut-off energy of 500 eV would provide accurate results, within 10^{-3} eV, and were kept consistent throughout. The Methfessel Paxton [24] smearing method (width 0.1 eV) was used and full geometry relaxations were carried out under constant pressure for all calculations. Collinear spin polarisation effects were included. For the exchange-correlation functional, the generalised gradient approximation as developed by Perdew-Burke-Ernzerho [25] (GGA-PBE) was utilised. The convergence criterion for electronic convergence was 10^{-6} eV and for geometry optimisation was 10^{-4} eV.

To simulate disordered and partially ordered solute clusters, supercells of 128 atoms with BCC packing were created and the lattice sites were occupied by random selection of the elements allowed in that sublattice. For example, in the B2 structure, Ni is restricted to one sublattice, Mn and Si are restricted to the other, and Fe pervades both. The randomisations were performed 10 times to produce 10 unique supercells of each composition providing a range of energies. This method has been used to much success in previous studies [26–28]. For the compositions analogous to the ferritic steel matrix of experimental specimens of A508 steels, single 250 atom supercells were used. For further methodology details please refer to a previous study [29].

3. Results and discussion

3.1. Effect of concentration of Mn, Ni and Si in α-Fe

In past experimental studies on RPV steels, through the use of APT, solute clusters are observed to evolve with increasing fluence [30]. To simulate this evolution, alloys with concentrations of 0, 50 and 66 at. % Fe, were investigated. The ratio of Mn:Ni:Si was fixed to 6:16:7 (stoichiometric G-phase). Three BCC packed structures, A2, B2 and $D0_3$ (Fig. 1), were investigated and compared to the G-phase intermetallic, which also had varying Fe contents. The $D0_3$ partial ordering was not found to differ from the fully disordered energies and therefore was not included in the results or investigated further.

The dilute ferrite matrix of three A508 RPV steel analogues are also simulated for comparison: (1) a grade 2 steel with comparatively high amounts of Mn, Ni and Si "ZV-806", (2) a grade 4 N steel that omits Si "123P171" and (3) a grade 4 N steel that omits Mn "Superclean". These three compositions were modelled after experimental specimens of details found in Refs. [31] and [32]; a summary of their compositions can be found in Table 1. It should be mentioned that the "omission" of Si and Mn in "123P171" and "Superclean", respectively, is due to their low levels <0.4 at. % of the alloying elements, which are therefore excluded from the 250 atom supercells.

In Fig. 2, it is seen that the formation enthalpy of each composition decreases (becomes more favourable) with the removal of Fe. It is evident that there is an energetic preference for the formation and enrichment of the solute clusters within the BCC configuration – an observation that supports the argument that the formation of solute clusters is radiation enhanced. The B2 partial ordering has a slight energetic preference (0.02–0.09 eV/at), which is increases with decreasing Fe, compared to the fully disordered A2 phase at 0 K. The G-phase is unstable at Fe contents of 25 and 50 at. % and a large degree of reconstruction, to strained G-phase geometries, occurs during geometry optimisation. The spread in energies of these structures is plotted in Fig. S1 (supplementary material) but is represented by a shaded region in Fig. 2. The G-phase is predicted to become energetically more stable than the BCC packing below a threshold Fe content between 10 and 18 at. % corresponding well to experimental observations of ~13 at. % by Matsukawa in duplex stainless steels [20].

It should be emphasised that the simulated fixed ratio of Mn, Ni and Si is idealised for ease of comparison to the stoichiometry of the G-phase and cluster compositions found in both duplex stainless steels and RPV steels can deviate significantly, as well as include other solute species [33,34].

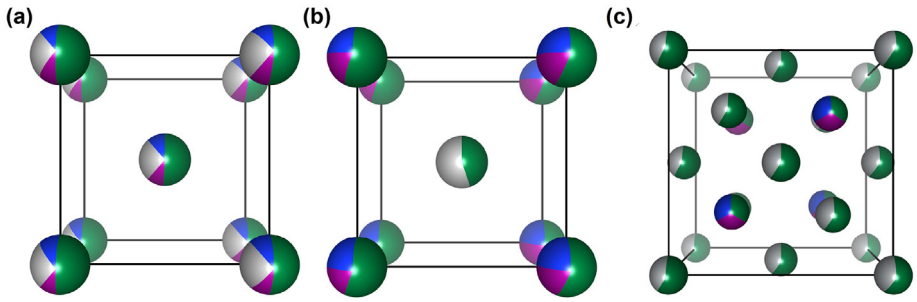

Fig. 1. Visual representation of the 50 at. % Fe structures with coloured site occupancy fractions in (a) A2, (b) B2 and (c) $D0_3$ partially ordered structures where Fe, Mn, Ni and Si are represented by green, purple, grey and blue, respectively. (For interpretation of the references to colour in this figure legend, the reader is referred to the Web version of this article.)

Table 1
Experimentally measured base metal concentration of Mn, Ni, Si and other elements within the previously studied steels; where Fe is the remainder (units are atomic ppm).

Steel	Mn	Ni	Si	Other
A508 Gr 2 (ZV-806) [31]	116	143	26.2	329
A508 Gr 4 N (123P171) [30]	54.9	758	2.9	501
Superclean A508 Gr 4 N (118K001) [30]	3.8	717	0.971	524

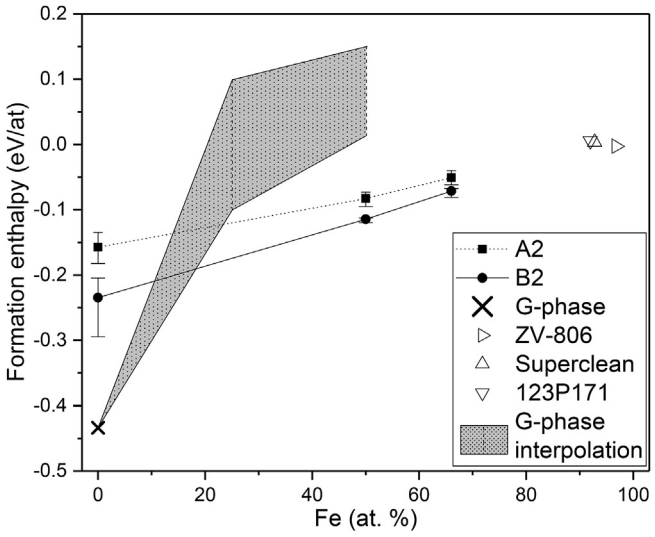

Fig. 2. Average formation enthalpies of the $Fe_xMn_6Ni_{16}Si_7$ A2 (filled squares) and B2 (filled circles) phases and their associated range in values (error bars), where x is varied from 0 to 66 at. %. The formation enthalpy of the G-phase, where $x = 0$ at. % (cross), and spread in energies at $x = 25$ and 66 at. % (dashed vertical lines) with the interpolated range of energies represented as a shaded region. Compositions indicative of the ferrite matrix of three experimentally characterised A508 specimens were also compared (open triangles).

3.2. B2 partial ordering of solute clusters in α-Fe

The similarity between the G-phase and B2 partial ordering is assessed within this section. Fig. 3 provides a visual representation of the similarities. Table S1 explicitly states the location of the lattice matched sites. Interestingly, all the Si atoms and half the Ni sites are lattice matched, with all the Mn atoms experiencing reconstruction to form the G-phase.

In contrast to the matching lattice sites between the cubic G-phase unit cell and the $4 \times 4 \times 4$ B2 structure, there are 12 fewer atoms in the former. The coordinates of these discrepant atoms are also stated in Table S1. If the atoms at these locations are removed from the B2 supercell, prior to geometry optimisation in DFT – the G-phase is the resultant structure. The vectors (to scale) corresponding to the atomic displacements made as a result of the geometry optimisation within DFT can be seen in Fig. 4.

The spontaneous phase transformation, in the DFT energy minimisation, from a defective BCC packed structure to G-phase is a significant result as the transformation from BCC → G-phase is hypothesised in experimental studies [20,35]. The current observation would suggest that the energy barriers for this transformation are dominated by the migration of the elements to their lattice matched sites and/or the formation of the twelve vacancies not the structural transformation itself, which is predicted to occur spontaneously once the preferred atomic ordering is present.

Within this study, all simulations included spin polarisation effects, and as a result a significant degree of magnetic disorder was observed. The distribution of magnetic moments for each element can be seen in Fig. 5 for the simulated disordered systems.

In absence of Fe, Ni exhibits negligible magnetisation, but with the addition of 50 and 66 at.% Fe, spin polarisation on the Ni atoms was observed. Following the trend seen in binary Fe-Ni alloys, Ni adopted a spin-aligned orientation relative to Fe with an average magnitude in magnetic moment smaller than that of a pure Fe-Ni alloy (~1 μ_B) [36]. Mn exhibited a more varied behaviour with a broad distribution of magnetic moments from −3 to 3 μ_B in both structures at 0 and 66 at. % Fe. There is clear localisation of the magnetic moment of Mn for the 50 at. % Fe content at 2.5–3 μ_B in both A2 and B2 but the B2 has a narrower distribution. It is well-known that Mn is highly susceptible to adopting a wide range of magnetic structures [37]; theoretical methods predict the local antiferromagnetic case to be more energetically favourable (in α-Fe) [38]. Furthermore, there is a shallow energy landscape between the high and low spin-state for Mn [39] in α-Fe. Indeed, within this study Mn is predicted to exhibit a large degree of disorder. The magnetic moment of Fe adopted a bimodal distribution in the B2 structures whereby the lower magnitudes correspond to the Fe atoms located on the Ni occupied sublattice. This behaviour is to be expected as the magnetic moment of Fe, in α-Fe (2.2 μ_B), deviates under the influence of solute atoms in their local environment [40].

3.3. Entropy

For highly alloyed mixtures of elements, the configurational entropy can contribute significantly to phase stability [41]. The vibrational and electronic components of entropy are predicted to contribute up to a maximum of half the magnitude of the configurational entropy [42,43]. When comparing two phases of the same packing and chemistry (with the only difference being site occupancies) the difference in vibrational entropy between the phases is expected to be small but non-negligible [44,45]. However, calculation of vibrational entropy for a large set of disordered systems is

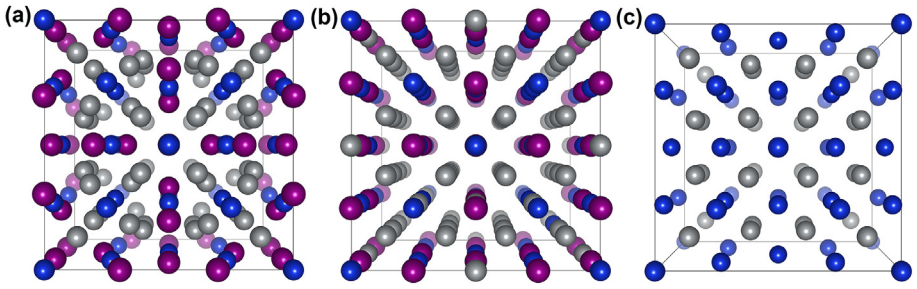

Fig. 3. Atomic representation Mn (purple), Ni (grey) and Si (blue) in a cubic (a) G-phase unit cell, (b) B2 ordered ($4 \times 4 \times 4$) supercell and (c) their lattice matched atomic sites. (For interpretation of the references to colour in this figure legend, the reader is referred to the Web version of this article.)

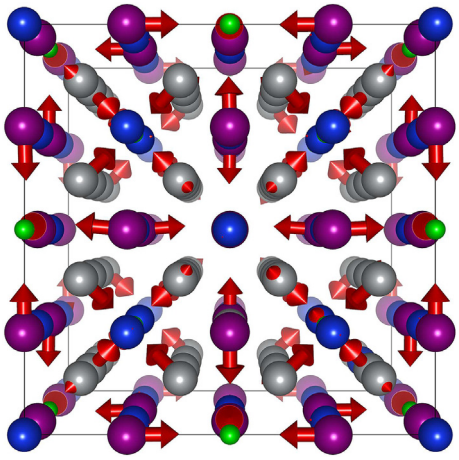

Fig. 4. Perfect B2 $4 \times 4 \times 4$ supercell with absences (green) and vectors (red) of the displacements predicted by DFT to obtain the G-phase. 3.3 Magnetic structure. (For interpretation of the references to colour in this figure legend, the reader is referred to the Web version of this article.)

currently computationally unfeasible. For this reason, we consider configurational and magnetic entropy only.

The magnitude of the configurational entropy is proportional to the degree of disorder. Above some threshold temperature, a fully disordered case will become energetically favourable (providing that temperature is below the solidus). In the case of the modelled A2 and B2 solute clusters this threshold temperature was obtained by equating the calculated Gibbs free energy of the two phases:

$$T_{thr} = \frac{H_{A2} - H_{B2}}{S_{A2} - S_{B2}} \tag{1}$$

where H_{A2} and H_{B2} are the average calculated formation enthalpies of the disordered and partially ordered structures at 0 K, respectively, and S_{A2} and S_{B2} are the sum of the configurational and magnetic entropies of the disordered and partially ordered structures, respectively. The configurational entropy of the fully disordered structure was calculated using the equation for Gibbs entropy [46]:

$$S_{A2} = -nR \sum_{i=1}^{N} x_i \ln(x_i) \tag{2}$$

where n is the number of moles, R is the gas constant and x_i is the atomic fraction of element i in an N element system. To calculate S_{B2}, the sublattices were treated as separate alloys weighted by their contribution to 1 mol of the combined system:

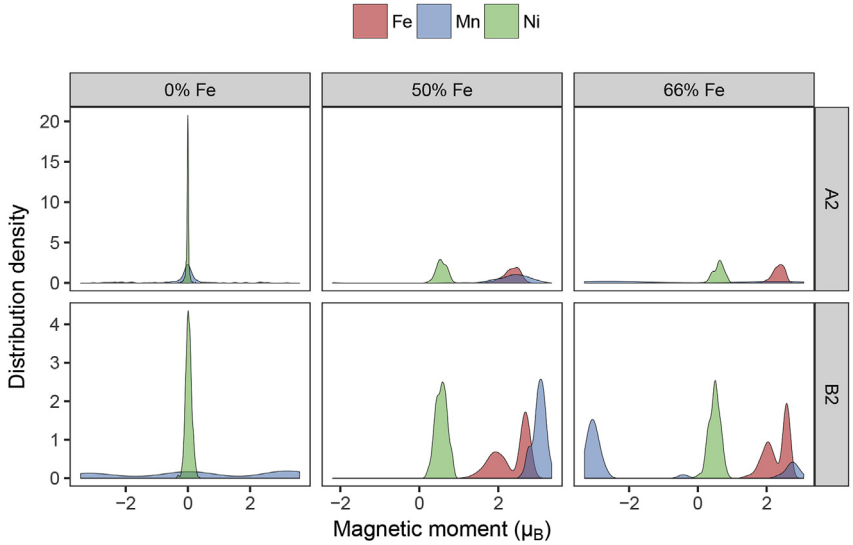

Fig. 5. The distribution of magnetic moments of Fe (red), Mn (green) and Ni (blue) in the A2 and B2 phases with varying Fe content. (For interpretation of the references to colour in this figure legend, the reader is referred to the Web version of this article.)

Table 2
Calculated configurational entropy (S_{conf}) and magnetic entropy (S_{mag}) of B2 and A2 solute clusters and the threshold temperature (T_{thr}) at which the two phases are in thermodynamic equilibrium ($G_{A2} = G_{B2}$).

Fe content (at. %)	S_{B2} ($\times 10^{-5}$ eV/at/K)		S_{A2} ($\times 10^{-5}$ eV/at/K)		T_{thr} (K)
	S_{conf}	S_{mag}	S_{conf}	S_{mag}	
0	4.13	1.87	8.57	1.36	1971
50	7.22	2.84	10.1	2.52	1202
66	6.36	2.56	8.37	2.62	985

$$S_{B2} = -R\left[\sum_{k=1}^{L} n_k \sum_{\substack{i=1 \\ i\neq\alpha}}^{N} x_{i,k}\ln(x_{i,k})\right] \quad (3)$$

where k is the sublattice in a system with L number of sublattices and α denotes any element that does not appear on that specific sublattice. This method has been used to much success in the past [27,47].

Magnetic entropy is estimated in much the same manner as the configurational entropy term [48] and represents the number of magnetic states possible for each elemental species to exist within each structure [49]. These states are taken from the DFT calculations (Fig. 4).

$$S_{B2} = -R\left[\sum_{i=1}^{N} n_i \sum_{s=1}^{M} X_{s,i}\ln(X_{s,i})\right] \quad (4)$$

where $X_{s,i}$ is the fraction of atoms of element i with the same magnetic moment, s, normalised to the total number of atoms of element i and M is the total number of atoms.

Within this study, $X_{s,i}$ was calculated from the density distribution seen in Fig. 5, discretised into fix-width bins of 0.03 μ_B width. Due to the continuous nature of the magnetic moments the magnetic entropies were logarithmically proportional to the bin size used. However, the relative change in entropy between A2 and B2 phases is independent of bin size.

The predicted entropy contributions and threshold temperatures above which the disordered solute clusters become more favourable than their partially ordered counterparts, can be seen in Table 2.

The magnetic contribution, to the total entropy, are of relatively similar magnitudes between the A2 and B2 structures; it is the configurational entropy that is predicted to have the greatest impact on phase stability.

The quoted values for T_{thr} are calculated using the *average* formation enthalpies of the A2 and B2 structures. By using a combination of minimum enthalpy of A2 and maximum enthalpy of B2, and vice-versa, a range in T_{thr} values are obtained: 524–4228 K, 711–1891 K and 679–1019 K for 0, 50 and 66 at. % Fe, respectively. For the 0 at. % Fe structures, it is reasonable to assume that this large degree of uncertainty arises due to the metastability of the BCC phase and that the threshold temperature is unphysical. For the structures with 50 and 66 at. % Fe, these results suggest that the B2 type ordering may be stable in the solute clusters at operating temperatures of the steel components. In experimental terms, it should be possible to identify such ordering using TEM. However, at the lower bounds of the estimated T_{thr} values the kinetics may be insufficient for ordering to occur.

3.4. In the context of RPV steels

The results within this study suggest that the clustering of Mn, Ni and Si is thermodynamically favourable in typical low alloy ferritic steels. However, past literature has shown that, at RPV operational temperatures, thermal effects alone are insufficient for clustering, therefore equilibrium, to occur [50]. The roles of neutron flux, fluence, and subsequently, non-equilibrium defects are not explored here in depth. Assuming that four conditions are met: (1) The increase of neutron fluence has the effect of driving the system to equilibrium, (2) a ratio of Mn:Ni:Si is 6:16:7 is achieved in the cluster, (3) the cluster reaches a size large enough to overcome an unfavourable surface energy, and (4) the Fe concentration drops below 10–18 at. % Fe – precipitation of the G-phase is predicted to occur. However, the occurrence of these conditions is currently in contention within the literature. If at least one of these assumptions are false, it is predicted that the clusters will remain BCC in either the A2 or B2 form. Transmission electron microscopy and electron diffraction can be used to identify and differentiate the three structures (A2, B2 and G-phase) provided the resolution is adequate and the features are sufficiently large (~2 nm).

The nature of the transition from BCC to G-phase is not known. However, we have shown that for a BCC packed structure of lattice matched 6Mn:16Ni:7Si stoichiometry, 12 vacancies in a 128 atom supercell will allow for a spontaneous reconstruction to the G-phase structure. The flux experienced by a typical RPV steel in operation is insufficient to induce a defect concentration of 9.38%; however, other kinetic processes such as defect and solute migration may play a role in this transition. Work in this area is ongoing.

4. Conclusions

The enrichment of solute species Mn, Ni and Si is energetically preferable over the dilute ferrite matrix of a typical low alloy steel. Below 10–18 at. % Fe, the G-phase is predicted to be more stable than BCC packing, in agreement with past experimental observations on duplex stainless steels.

The energy barrier for transformation from BCC packing to G-phase is expected to exist in the vacancy production and migration of solute species. When ~10% of vacancies are introduced into the BCC structure (12 vacancies in a 128-atom supercell), and elemental site occupancies are lattice matched, the transformation from between the BCC → G-phase is expected to occur spontaneously.

At 0 K the B2 partial ordering is more energetically favourable than the A2 configuration at all Fe contents of the solute clusters. When considering the configurational and magnetic entropy, the A2 structure will become energetically favourable at composition specific threshold temperatures. Magnetic entropy is determined to be significantly less important than configurational entropy in the order/disorder transition of A2/B2.

Acknowledgements

Mark Wenman and Daniel King were funded by EPSRC grant no. EP/P005101/1. M. Grace Burke is funded by grant no. EP/P003591/1. Thomas Whiting acknowledges support through the CDT in nuclear energy grant no. EP/L015900/1 and funding from Rolls-Royce Plc. This research was undertaken with the assistance of resources

provided by the Australian National Computational Infrastructure supported by Intersect Australia Ltd (Raijin) and Imperial College Tier 2 computing (Cx1 and Cx2).

Appendix A. Supplementary data

Supplementary data related to this article can be found at https://doi.org/10.1016/j.jnucmat.2018.03.050.

References

[1] H.J. Beattie, F.L. VerSnyder, A new complex phase in a high-temperature alloy, Nature 178 (1956) 208–209.
[2] J.M. Vitek, G-phase formation in aged type 308 stainless steel, Metall. Trans. A. 18 (1987) 154–156.
[3] K.H. Lo, C.H. Shek, J.K.L. Lai, Recent developments in stainless steels, Mater. Sci. Eng. R Rep. 65 (2009) 39–104.
[4] M.K. Miller, J. Bentley, APFIM and AEM investigation of CF8 and CF8M primary coolant pipe steels, Mater. Sci. Technol. 6 (1990) 285–292.
[5] F. Gillemot, Overview of reactor pressure vessel cladding, Int. J. Nucl. Knowl. Manag. 4 (2010) 265–278.
[6] S.J. Zinkle, G.S. Was, Materials challenges in nuclear energy, Acta Mater. 61 (2013) 735–758.
[7] S.J. Zinkle, J.T. Busby, Structural materials for fission & fusion energy, Mater. Today 12 (2009) 12–19.
[8] R. Ngayam-Happy, C.S. Becquart, C. Domain, L. Malerba, Formation and evolution of MnNi clusters in neutron irradiated dilute Fe alloys modelled by a first principle-based AKMC method, J. Nucl. Mater. 426 (2012) 198–207.
[9] J.F. Knott, C.A. English, D.R. Weaver, D.P.G. Lidbury, Views of TAGSI on the effects of gamma irradiation on the mechanical properties of irradiated ferritic steel reactor pressure vessels, Int. J. Pres. Ves. Pip. 82 (2005) 929–940.
[10] G.R. Odette, T. Yamamoto, D. Klingensmith, On the effect of dose rate on irradiation hardening of RPV steels, Philos. Mag. A 85 (2005) 779–797.
[11] P. Pareige, J.C. Van Duysen, P. Auger, An APFIM study of the microstructure of a ferrite alloy after high fluence neutron irradiation, Appl. Surf. Sci. 67 (1993) 342–347.
[12] J.M. Hyde, A. Cerezo, T.J. Williams, Statistical analysis of atom probe data: detecting the early stages of solute clustering and/or co-segregation, Ultramicroscopy 109 (2009) 502–509.
[13] M.K. Miller, K.A. Powers, R.K. Nanstad, P. Efsing, Atom probe tomography characterizations of high nickel, low copper surveillance RPV welds irradiated to high fluences, J. Nucl. Mater. 437 (2013) 107–115.
[14] ASTM International, Standard specification for quenched and tempered vacuum-treated carbon and alloy steel forgings for pressure vessels BT - standard specification for quenched and tempered vacuum-treated carbon and alloy steel forgings for pressure vessels, in: World Trade Organization TBT Committee, 2017. West Conshohocken, PA.
[15] G.R. Odette, G.E. Lucas, Recent progress in understanding reactor pressure vessel steel embrittlement, Radiat. Eff. Defect Solid 144 (1998) 189–231.
[16] H. Ke, P. Wells, P.D. Edmondson, N. Almirall, L. Barnard, G.R. Odette, D. Morgan, Thermodynamic and kinetic modeling of Mn-Ni-Si precipitates in low-Cu reactor pressure vessel steels, Acta Mater. 138 (2017) 10–26.
[17] G. Odette, B. Wirth, A computational microscopy study of nanostructural evolution in irradiated pressure vessel steels, J. Nucl. Mater. 251 (1997) 157–171.
[18] X. Yan, A. Grytsiv, P. Rogl, V. Pomjakushin, X. Xue, On the crystal structure of the Mn–Ni–Si G-phase, J. Alloy. Comp. 469 (2009) 152–155.
[19] S. Li, Y. Wang, X. Wang, F. Xue, G-phase precipitation in duplex stainless steels after long-term thermal aging: a high-resolution transmission electron microscopy study, J. Nucl. Mater. 452 (2014) 382–388.
[20] Y. Matsukawa, T. Takeuchi, Y. Kakubo, T. Suzudo, H. Watanabe, H. Abe, T. Toyama, Y. Nagai, The two-step nucleation of G-phase in ferrite, Acta Mater. 116 (2016) 104–113.
[21] B. Gault, M.P. Moody, J.M. Cairney, S.P. Ringer, Atom Probe Microscopy, Springer Science & Business Media, 2012.
[22] G. Kresse, J. Furthmüller, Software VASP, vienna, Phys. Rev. B 54 (1996) (1999) 169.
[23] G. Kresse, D. Joubert, From ultrasoft pseudopotentials to the projector augmented-wave method, Phys. Rev. B 59 (1999) 1758.
[24] M. Methfessel, A.T. Paxton, High-precision sampling for Brillouin-zone integration in metals, Phys. Rev. B 40 (1989) 3616.
[25] J.P. Perdew, K. Burke, M. Ernzerhof, Generalized gradient approximation made simple, Phys. Rev. Lett. 77 (1996) 3865.
[26] S.C. Middleburgh, D.M. King, G.R. Lumpkin, M. Cortie, L. Edwards, Segregation and migration of species in the CrCoFeNi high entropy alloy, J. Alloy. Comp. 599 (2014) 179–182.
[27] D.M. King, S.C. Middleburgh, L. Edwards, G.R. Lumpkin, M. Cortie, Predicting the crystal structure and phase transitions in high-entropy alloys, JOM (J. Occup. Med.) 67 (2015) 2375–2380.
[28] D.J.M. King, S.C. Middleburgh, A.G. McGregor, M.B. Cortie, Predicting the formation and stability of single phase high-entropy alloys, Acta Mater. 104 (2016) 172–179.
[29] D.J.M. King, P.A. Burr, E.G. Obbard, S.C. Middleburgh, DFT study of the hexagonal high-entropy alloy fission product system, J. Nucl. Mater. 488 (2017) 70–74.
[30] P.B. Wells, T. Yamamoto, B. Miller, T. Milot, J. Cole, Y. Wu, G.R. Odette, Evolution of manganese–nickel–silicon-dominated phases in highly irradiated reactor pressure vessel steels, Acta Mater. 80 (2014) 205–219.
[31] M.G. Burke, R.J. Stofanak, M. Hyde, C.A. English, W.L. Server, Microstructural aspects of irradiation damage in A508 Gr 4N forging steel: composition and flux effects, in: M.L. A. Grossbeck, T.R. Allen, R.G. Lott, Kumar (Eds.), Eff. Radiat. Mater. 21st Int. Symp, American Society Testing and Materials, 2004, pp. 194–207.
[32] M.G. Burke, R.J. Stofanak, J.M. Hyde, C.A. English, W.L. Server, Characterisation of irradiation damage in A508 class 2 and class 4 forging steels, in: G.S. Was, L. Nelson (Eds.), 10th Int. Symp. Environ. Degrad. Mater. Nucl. Power Syst. React, 2002.
[33] T. Takeuchi, J. Kameda, Y. Nagai, T. Toyama, Y. Matsukawa, Y. Nishiyama, K. Onizawa, Microstructural changes of a thermally aged stainless steel submerged arc weld overlay cladding of nuclear reactor pressure vessels, J. Nucl. Mater. 425 (2012) 60–64.
[34] T. Takeuchi, Y. Kakubo, Y. Matsukawa, Y. Nozawa, T. Toyama, Y. Nagai, Y. Nishiyama, J. Katsuyama, Y. Yamaguchi, K. Onizawa, Effects of thermal aging on microstructure and hardness of stainless steel weld-overlay claddings of nuclear reactor pressure vessels, J. Nucl. Mater. 452 (2014) 235–240.
[35] T. Hamaoka, A. Nomoto, K. Nishida, K. Dohi, N. Soneda, Accurate determination of the number density of G-phase precipitates in thermally aged duplex stainless steel, Philos. Mag. A 92 (2012) 2716–2732.
[36] M.F. Collins, J.B. Forsyth, The magnetic moment distribution in some transition metal alloys, Philos. Mag. A 8 (1963) 401–410.
[37] D. Hobbs, J. Hafner, Density functional study of phase stability and noncollinear magnetism in Mn, J. Phys. Condens. Matter 13 (2001) L681–L688.
[38] H. Akai, M. Akai, J. Kanamori, Electronic structure of impurities in ferromagnetic iron. II. 3d and 4d impurities, J. Phys. Soc. Japan 54 (1985) 4257–4264.
[39] B. Drittler, N. Stefanou, S. Blügel, R. Zeller, P.H. Dederichs, Electronic structure and magnetic properties of dilute Fe alloys with transition-metal impurities, Phys. Rev. B 40 (1989) 8203.
[40] A. Ayuela, N.H. March, The magnetic moments and their long-range ordering for Fe atoms in a wide variety of metallic environments, Int. J. Quant. Chem. 110 (2010) 2725–2733.
[41] D. Ma, B. Grabowski, F. Körmann, J. Neugebauer, D. Raabe, Ab initio thermodynamics of the CoCrFeMnNi high entropy alloy: importance of entropy contributions beyond the configurational one, Acta Mater. 100 (2015) 90–97.
[42] A. van de Walle, G. Ceder, The effect of lattice vibrations on substitutional alloy thermodynamics, Rev. Mod. Phys. 74 (2002) 11–45.
[43] A. Benisek, E. Dachs, The vibrational and configurational entropy of disordering in Cu_3Au, J. Alloy. Comp. 632 (2015) 585–590.
[44] T. Hickel, B. Grabowski, F. Körmann, J. Neugebauer, Advancing density functional theory to finite temperatures: methods and applications in steel design, J. Phys. Condens. Matter 24 (2011) 53202.
[45] F. Körmann, Y. Ikeda, B. Grabowski, M.H.F. Sluiter, Phonon broadening in high entropy alloys, Npj Comput. Mater 3 (2017) 36.
[46] R. Swalin, Thermodynamics of Solids, Wiley, New York, 1991, p. 21.
[47] C. Niu, A.J. Zaddach, A.A. Oni, X. Sang, J.W. Hurt, J.M. LeBeau, C.C. Koch, D.L. Irving, Spin-driven ordering of Cr in the equiatomic high entropy alloy NiFeCrCo, Appl. Phys. Lett. 106 (2015) 161906.
[48] M.S. Ghiorso, Thermodynamic analysis of the effect of magnetic ordering on miscibility gaps in the Fe– Ti cubic and rhombohedral oxide minerals and the Fe– Ti oxide geothermometer, Phys. Chem. Miner. 25 (1997) 28–38.
[49] B. Fultz, Vibrational thermodynamics of materials, Prog. Mater. Sci. 55 (2010) 247–352.
[50] M. Miller, K. Russell, Embrittlement of RPV steels : an atom probe tomography perspective, J. Nucl. Mater. 371 (2007) 145–160.